REPORT DOCUMENTATION PAGE

Form Approved
OMB No. 074-0188

1. AGENCY USE ONLY (Leave blank)	2. REPORT DATE	3. REPORT TYPE AND DATES COVERED
	April 13, 2005	Final Technical (08/1/02-12/31/04)

4. TITLE AND SUBTITLE
Synthesis of Multifunction Materials

5. FUNDING NUMBERS
Grant #N00014-02-1-0929

6. AUTHOR(S)
Hadis Morkoç, Ph.D.

7. PERFORMING ORGANIZATION NAME(S) AND ADDRESS(ES)
Virginia Commonwealth University
School of Engineering
PO Box 843068
Richmond, VA 23284-3068

8. PERFORMING ORGANIZATION REPORT NUMBER
Final Technical for #528811

9. SPONSORING / MONITORING AGENCY NAME(S) AND ADDRESS(ES)
Office of Naval Research
Program Officer, Colin E. Wood
ONR Code 312
Ballston Center Tower One
800 N. Quincy St., Arlington, VA 22217

10. SPONSORING / MONITORING AGENCY REPORT NUMBER

11. SUPPLEMENTARY NOTES

12a. DISTRIBUTION / AVAILABILITY STATEMENT
APPROVED FOR PUBLIC RELEASE; distribution is Unlimited

12b. DISTRIBUTION CODE

13. ABSTRACT *(Maximum 200 Words)*

Perovskite phase of PZT films have been formed on sapphire substrates and $Pt/Ti/SiO_2/Si$ and $Ir/Ti/SiO_2/Si$ substrates by RF sputtering and sol gel techniques. Structural, in the form of X-ray diffraction, optical in the form of absorption/transmission and spectroscopic ellipsometry, scanning electron microscopy (SEM), energy dispersive spectroscopy (EDS), and electrical measurements, in the form of polarization vs. electric field (or voltage) in capacitors have been performed. For electrical characterization, the top electrodes for Au/PZT/Pt and Au/PZT/Ir capacitors were fabricated by photolithography and liftoff process. The Ir bottom electrodes were obtained from Samsung Advanced Institute of Technology as part of a collaborative effort. The photolithography and wet etching conditions (HF, $HF:H_2O_2:HNO_3$) were optimized to explore scheduled multifunctional device applications. The polarization hysteresis and fatigue characteristics were measured by using a ferroelectric tester. In order to prepare better quality perovskite film, all the necessary source and other configurational modifications have been completed in oxides MBE and growth runs are eminent.

14. SUBJECT TERMS	15. NUMBER OF PAGES
Perovskites, PZT, oxides	29
	16. PRICE CODE

17. SECURITY CLASSIFICATION OF REPORT	18. SECURITY CLASSIFICATION OF THIS PAGE	19. SECURITY CLASSIFICATION OF ABSTRACT	20. LIMITATION OF ABSTRACT
Unclassified	Unclassified	Unclassified	SAR

Technical Objectives

Growth and characterization of a class of ferroelectric oxides for multifunctional device applications.

Technical Approach

In order to apply lead zirconate titanate (PZT) to functional devices such as sensors, surface acoustic wave (SAW) devices, metal ferroelectric semiconductor field effect transistors (MFSFETs) by utilizing wideband gap semiconductors like GaN, ZnO, etc., as essential steps, PZT thin films with various compositions (Pb:Zr:Ti ratio) were grown by RF sputtering and sol-gel techniques on various substrates, including sapphire, $Pt/Ti/SiO_2/Si$ and $Ir/Ti/SiO_2/Si$ substrates. Structural and optical characterizations were carried out by X-ray diffraction (XRD), scanning electron microscopy (SEM), energy dispersive spectroscopy (EDS), optical transmittance spectroscopy, and spectroscopic ellipsometry (SE) with varying diverse experimental parameters. We measured the dielectric functions of PZT, PNZT, PLZT, and PLT using SE covering infrared (IR), visible (VIS), ultraviolet (UV), and deep-ultraviolet (DUV) spectral range. VIS and UV data were obtained at Kyung Hee University in collaboration with Prof. Hoşun Lee, and IR and DUV were taken at University of Nebraska in collaboration with Prof. Paul Snyder and Prof. John Woollam. SE can estimate electronic and phonon band structures as well as refractive indices and thicknesses. Electronic band structure calculations are being performed by Dr. Su-hwai Wei at National Renewable Energy Laboratory. For electrical characterization, the top electrodes for Au/PZT/Pt and Au/PZT/Ir capacitors were fabricated by photolithography and liftoff process. The Ir bottom electrodes were obtained from Samsung Advanced Institute of Technology as part of a collaborative effort. The photolithography and wet etching conditions (HF, $HF:H_2O_2:HNO_3$) were optimized to explore scheduled multifunctional device applications. The polarization hysteresis and fatigue characteristics were measured by using a ferroelectric tester.

Progress

PZT growth by RF magnetron sputtering and characterizations

We have grown PZT films on sapphire substrates by RF sputtering (Fig. 1) under the condition tabulated in Table I. From point a to g through the region B, energy dispersive spectroscopy (EDS) analysis showed that the PZT composition is Pb = 24.57±2.52 (atomic %), Zr=3.17±0.52, Ti=2.64±1.28, O=69.63±3.02 (Table II), i.e. the atomic ratio between metallic elements Pb:Zr:Ti = 80.9:10.4:8.7 (Pb-rich condition), probably indicating that the sample consists of pyrochlore phase ($A_2B_2O_{7-\delta}$; A=Pb, B=Zr or Ti for PZT) + α-PbO (low temperature tetragonal phase). This sample denoted as PZT_PbO hereafter.

Fig. 2 shows XRD patterns associated with a half of 2 inch wafer (region A, B, C shown in Fig. 1). Only a relatively broad peak at $2\theta \approx 29^\circ$ and a very sharp sapphire substrate (reference) peak at $2\theta = 41.7^\circ$ were identified. No perovskite [e.g. PZT (011) or (111)] related peaks were observed, implying that heterogeneous nucleation on sapphire substrate did not occur during RF sputter growth. As shown in Fig. 3, the $2\theta \approx 29.2^\circ$ peak from region A can be fit with at least three line components (in this case asymmetric lines, $2\theta = 28.48^\circ$, 28.90°, and 29.18°), which are assigned to the pyrochlore (222) phase mixed with α-PbO_x (101) phase.

After rapid thermal annealing (RTA) at 750°C for 4 min in air, peaks near $2\theta \approx 29.2^\circ$ vanished and only sapphire substrate peak remained for most films as shown in Fig. 4. According to the phase diagram showing PbO pressure vs. temperature [Phys.Rev.Lett. 88, 016101 (2002)], the PbO is volatile (vapor phase) at 750°C, and thus, it is understood that the composition of as-grown PZT_PbO is mainly PbO with relatively small amount of pyrochlore phase, and PbO has evaporated during RTA. In order to optimize the composition (Pb:Zr:Ti ratio), small Zr (size: 6×3 mm) and Ti pellets (3×3 mm) were placed on top of the PZT sputtering target and co-sputtered during sputtering as illustrated in Fig. 5. When 3 Zr pellets and 10 Ti pellets were used, the composition of as-grown film was $Pb(Zr_{0.82}Ti_{0.18})O_3$ (denoted PZT82). Comparatively, Fig. 6 shows XRD patterns of as-grown PZT_PbO (PbO-rich) and PZT82 before and after RTA. The peak of PZT82 at $2\theta = 29.2^\circ$ becomes rather sharp and more asymmetric than that of PZT_PbO, but a little noticeable difference was observed. On the other hand, after RTA (800°C, 10 min in air), a perovskite PZT (110) ($2\theta = 31.3^\circ$) peak is clearly seen, indicating that phase transformation occured from pyrochlore to perovskite PZT during the RTA. When more Ti pellets (20 Ti and 3 Zr) were used, EDS analysis of the as-grown film clearly shows increased Ti composition in the film through the sample points 1 to 5 and the average film composition that was obtained to be $Pb(Zr_{0.56}Ti_{0.44})O_3$ (denoted PZT56) (Fig. 7 and Table III).

Fig. 8 compares the XRD of PZT82 and PZT56 before and after 800°C, 10 min RTA. As-grown PZT56 has the pyrochlore phase at $2\theta = 34.4^\circ$ (note the pyrochlore peak of PZT82 is at $2\theta = 29.2^\circ$), while RTA PZT56 clearly shows perovskite PZT with (111) orientation at $2\theta = 38.4^\circ$. These results show that one can drastically modify the composition and crystalline orientation of PZT (different orientation may be related to variation in Zr/Ti ratio) grown on sapphire by changing growth and/or anneal conditions in a manner employed in this work.

Fig. 9 shows the normalized transmittance data (semilog scale) of various as-grown and annealed PZT films: as-grown PZT_PbO (red), another measurement position on as-grown PZT_PbO (orange), as-grown PZT82 (green); PZT82 (furnace anneal at 800oC for 2hr in air, violet), PZT82 (RTA at 800oC for 10 min in air, brown), another measurement position on PZT82 (RTA at 800C for 10 min in air, black), PZT82 (furnace anneal at 800oC for 2hr, blue). The main difference between the violet and blue lines is the film thickness, i.e. 1500Å and 1000 Å, respectively. It is clearly seen that the absorption edge increases in the order of the as-grown PZT_PbO < the as-grown PZT82 < the annealed PZT82 (furnace annealing and/or RTA), i.e. the optical band gap increases in the same order. There are no noticeable differences between 10min RTA (in brown and in black) and 2hr furnace annealed PZT82 (in violet). The modulations below the absorption edge come from the interference fringes caused by the multiple reflections of the beam. The blue curve shows less interference and a relatively broad absorption edge compared to the other heat-treated sample (PZT82), probably because the sample is thinner as described.

Fig. 10(a) and (b) show the estimated band gap of the as-grown (green line in Fig. 9) and RTA PZT82 (black in Fig. 9). The two fitting (exponential) lines give band gaps of 2.857 eV for as-grown PZT82 and 3.518

eV for RTA PZT82, respectively. The latter corresponds to that of the PZT phase with perovskite structure (3.4 ~ 3.8 eV), favorable for ferroelectric applications.

Fig. 11 shows the transmittance data of RTA PZT82 (in black) and RTA PZT56 (in red) for comparision. It is seen that sample PZT56 has a steeper slope around the band edge than that seen in PZT82, which may be related to a lower defect concentration near the optical band edge in PZT56 compared to PZT82. For a clear understanding of this, further and detailed characterization is needed.

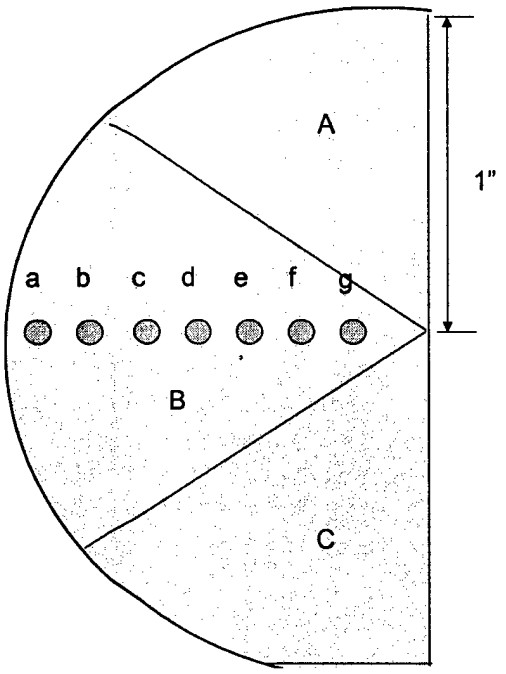

Table I: Growth condition

Heater temp. (°C)	750
Sample temp. (nominal)	411
Ar (sccm)	40
O_2	20
Pressure (mTorr)	1.35
T-S distance (cm)	10
RF power (W)	200

Table II: Average composition (EDS): point "a" through point "g"

Pb	24.57 ? 2.52 %
Zr	3.17 ? 0.52
Ti	2.64 ? 1.28
O	69.63 ? 3.02

Figure 1. Sample dimension: half of 2" sapphire wafer.
Table I. RF sputtering growth condition
Table II. Average composition (EDS) through point "a" and point "g" in region B.

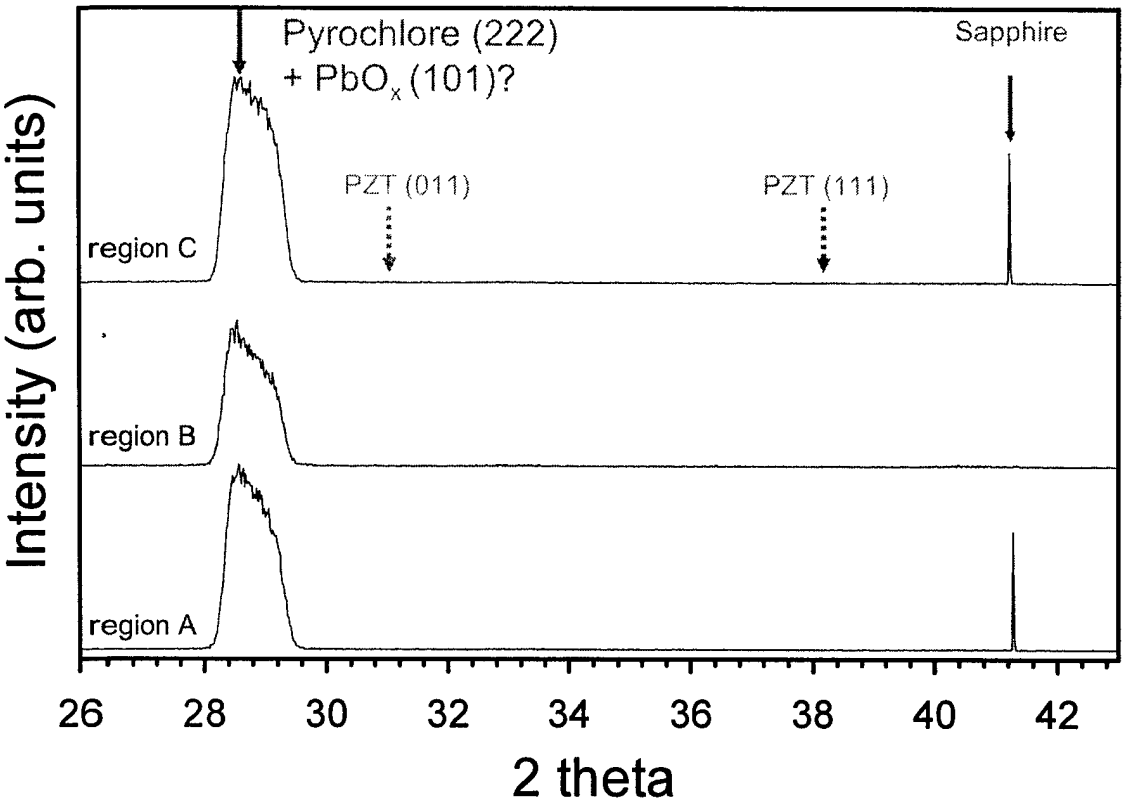

Figure 2. XRD of region A, B, and C of sample PZT_PbO.

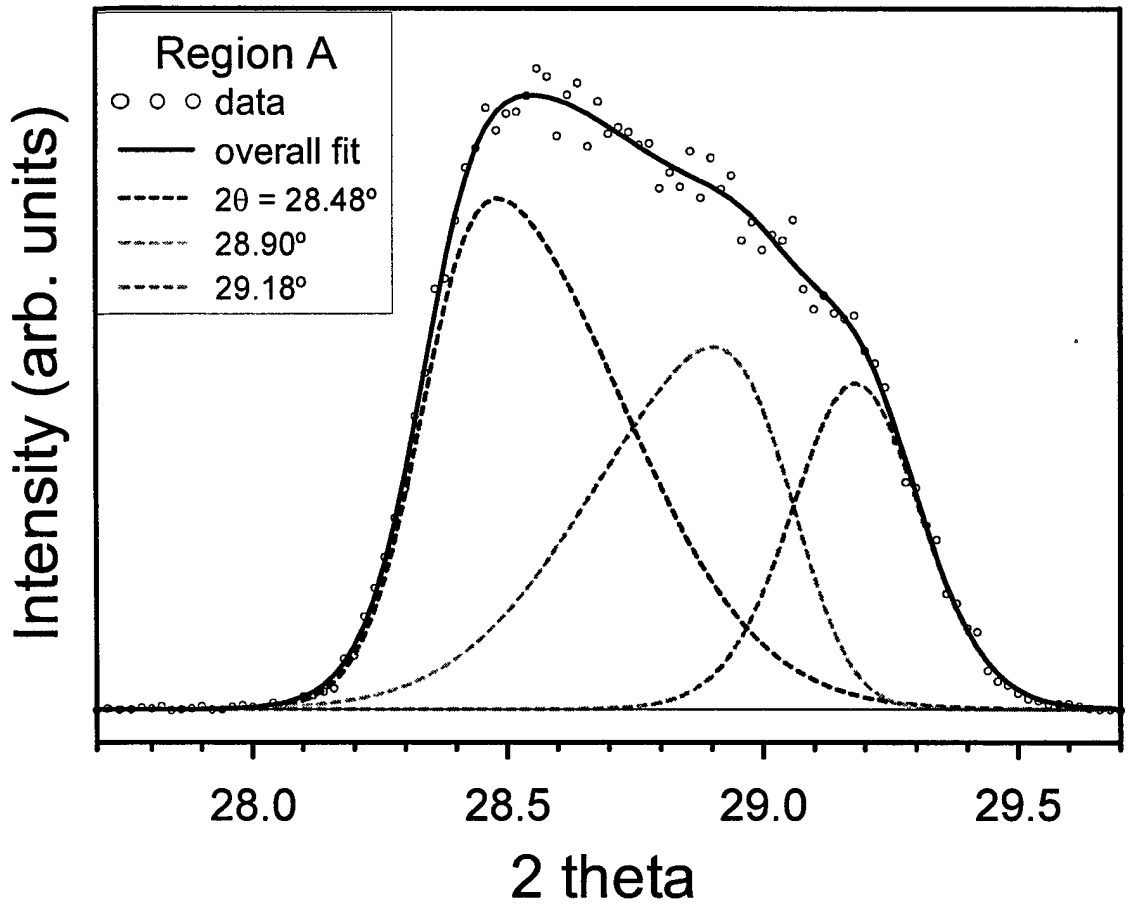

Figure 3. Curve fitting of near $2\theta \approx 29^{\circ}$ XRD peak (region A).

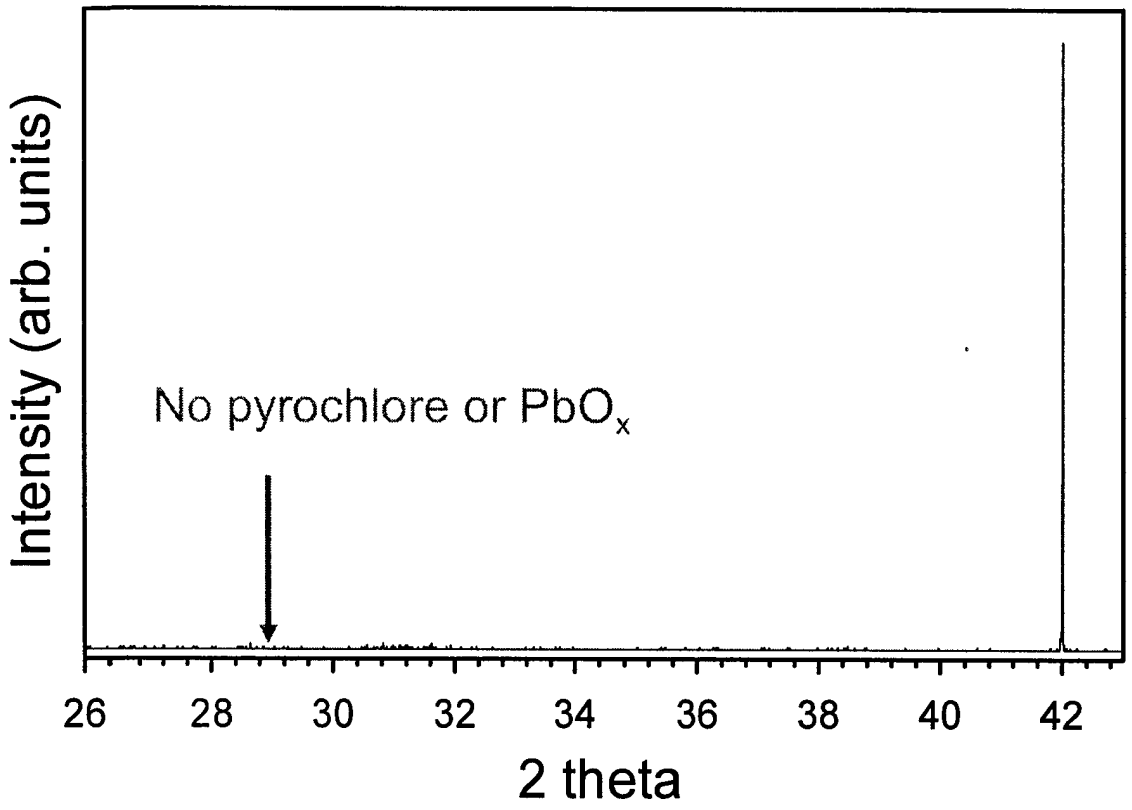

Figure 4. XRD of PZT_PbO (region A) after RTA at 750°C for 4min in air.

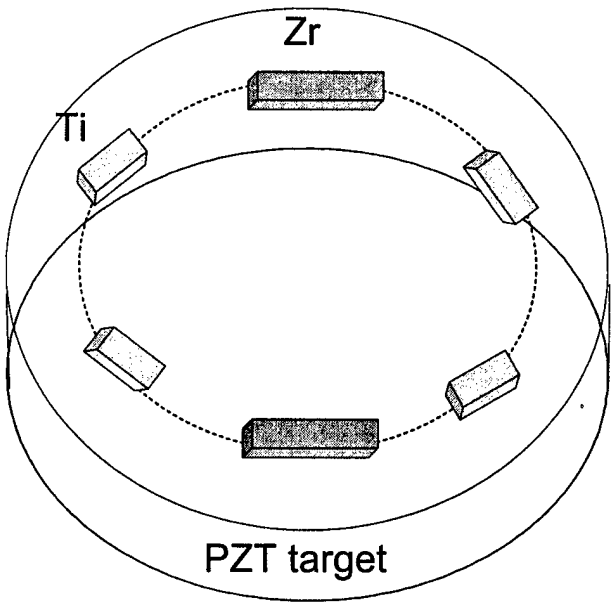

Figure 5. Schematic target configuration utilizing Zr and Ti pellets.

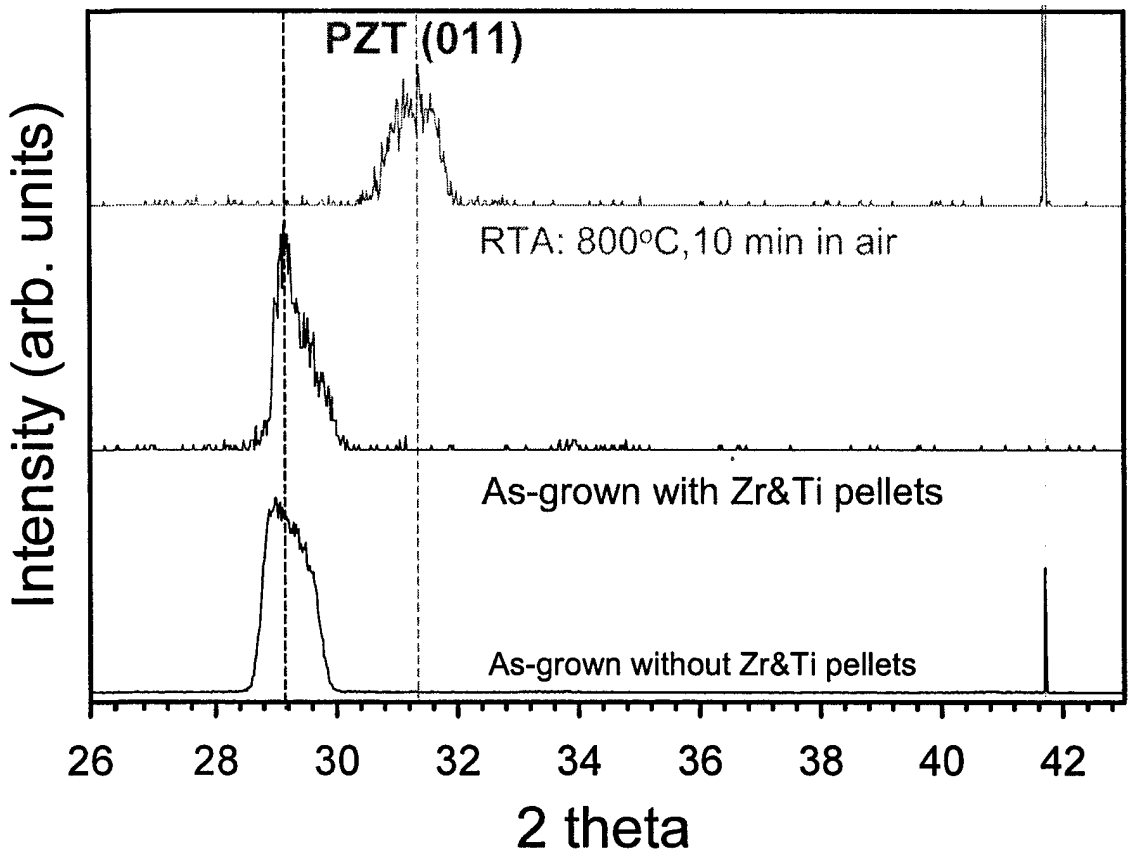

Figure 6. XRD of as-grown PZT_PbO, and as-grown and RTA PZT82 (800°C, 10 min in air).

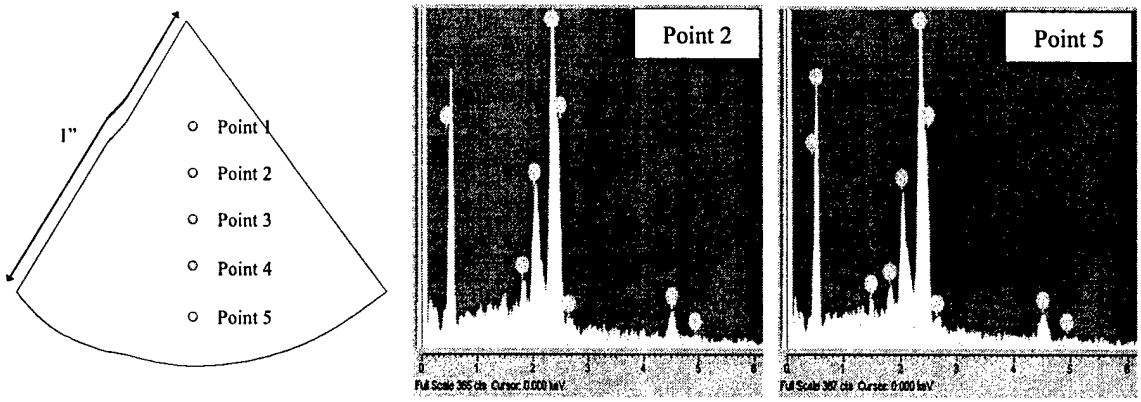

(a) (b)

Table III. Metallic element ratio (at%)

	Point 1	Point 2	Point 3	Point 4	Point 5	Average (Point 1~5)	Std. dev. (2σ)
Ti	**21.3**	**22.9**	**24.4**	**21.6**	**21.7**	**22.4**	1.3
Zr	30.1	29.3	26.1	29.9	28.0	**28.7**	1.7
Pb	48.6	47.8	49.5	48.5	50.3	**48.9**	1.0

Figure 7. (a) Shape of sample PZT56 (b) EDS of point 2 and point 5 showing Ti peaks

Table III. EDS average composition (metallic element ratio) of RTA PZT56 (800°C, 10 min in air).

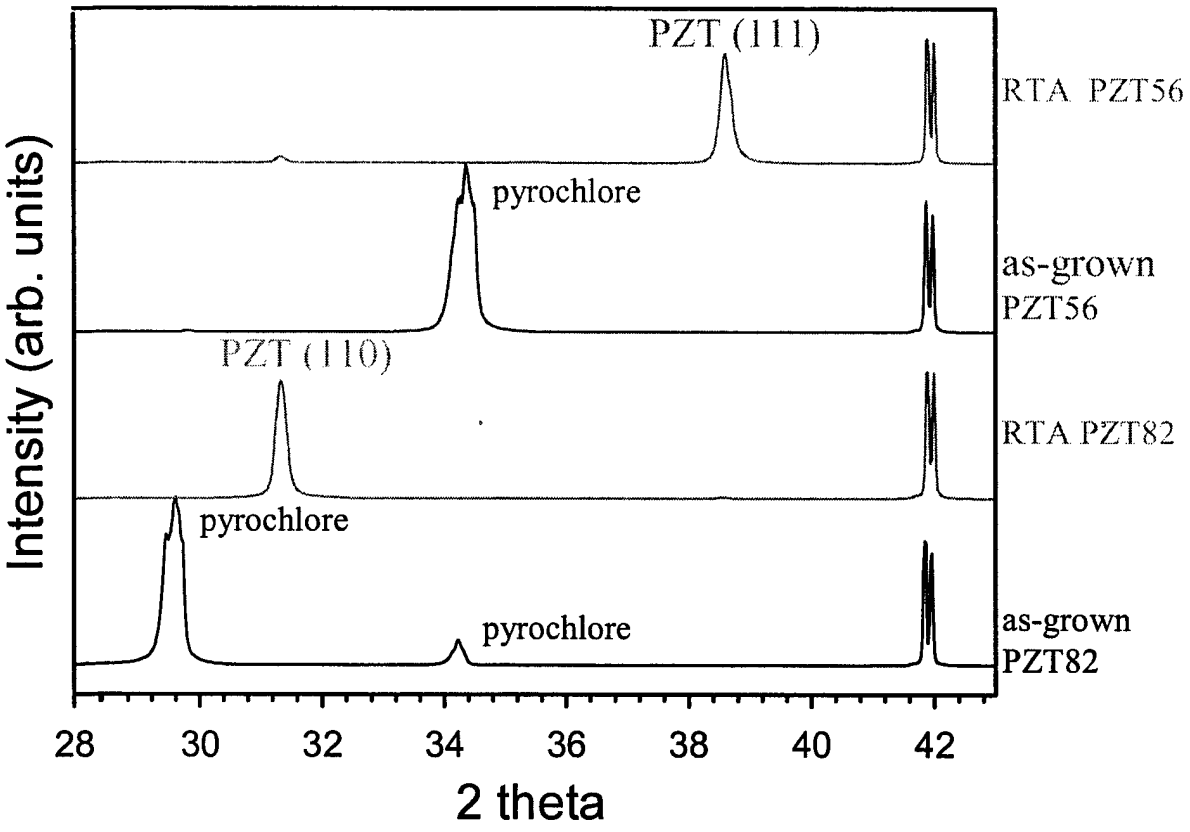

Figure 8. XRD of PZT82 and PZT56 before/ after RTA at 800°C for 10 min in air.

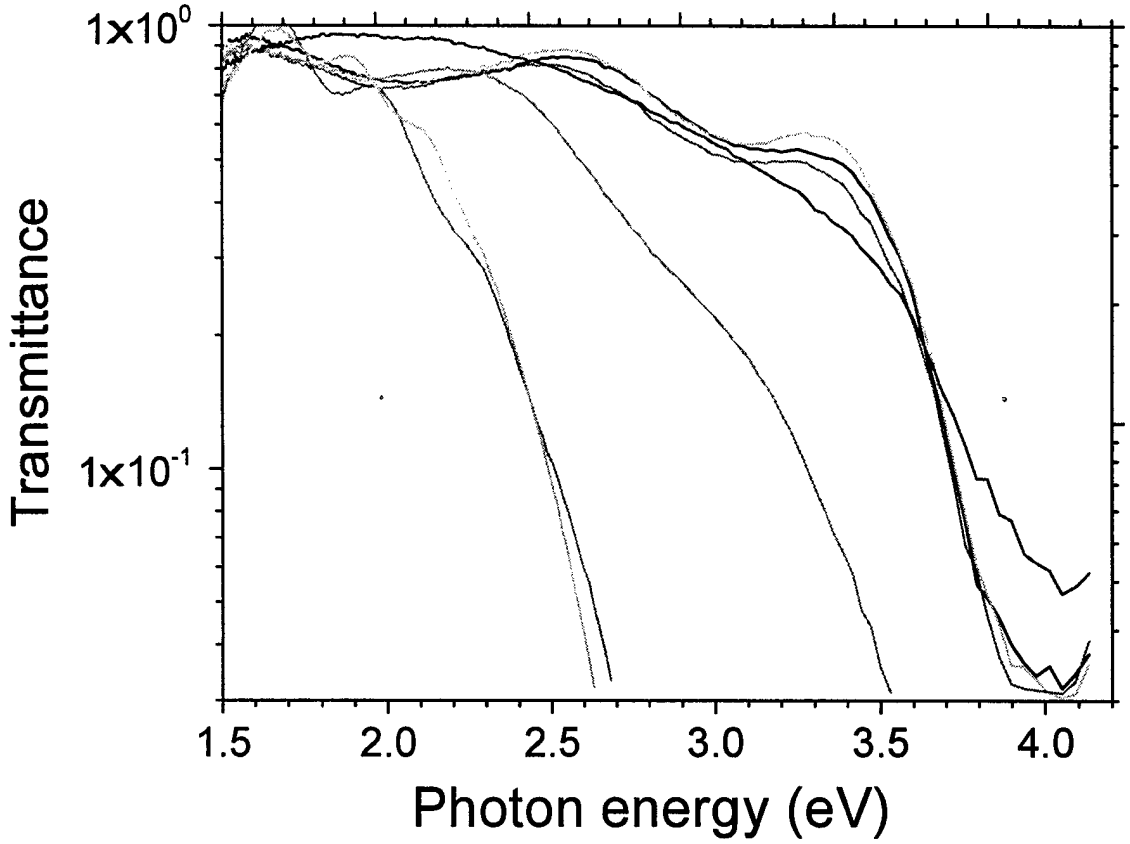

Figure 9. Transmittance of as-grown PZT_PbO, and PZT82 and PZT56 before and after RTA at 800°C for 10 min in air: [Red line] as-grown PZT_PbO; [Orange] another position on as-grown PZT_PbO; [Green] as-grown PZT82; [Violet] PZT82 (furnace anneal at 800°C for 2hr in air); [Brown] PZT82 (RTA at 800°C for 10 min in air); [Black] another position on PZT82 (RTA at 800C for 10 min in air); [Blue] PZT82 (furnace anneal at 800°C for 2hr).

(a)

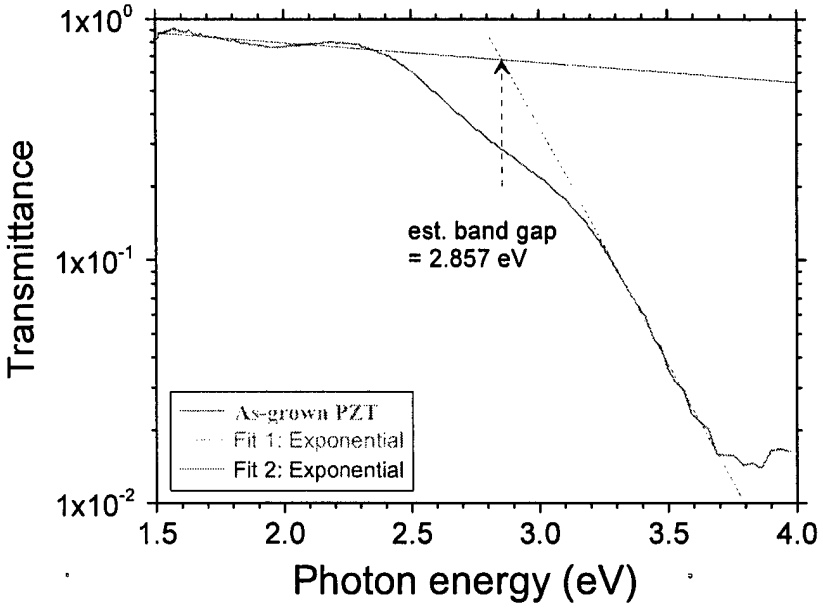

(b)

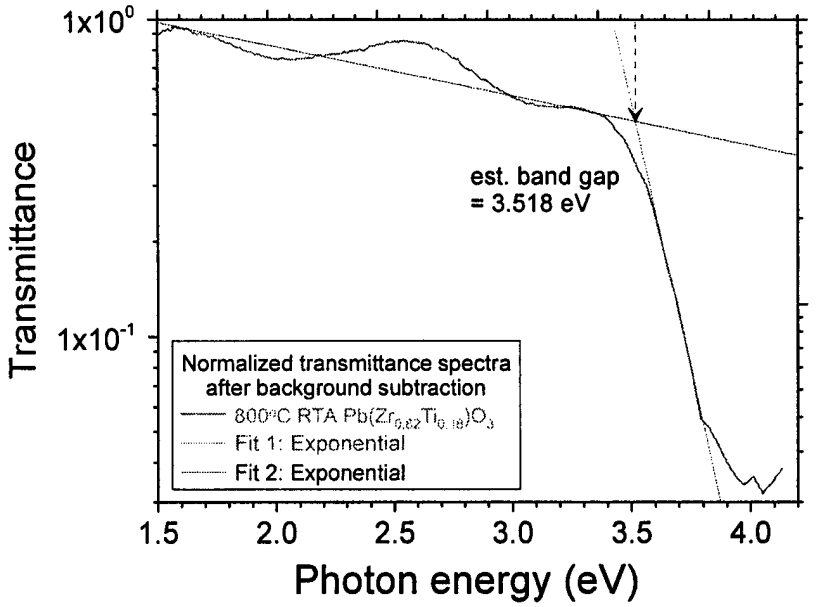

Figure 10. Estimation of band gap from transmittance data of (a) as-grown PZT_PbO and (b) PZT56 (RTA at 800°C for 10 min in air).

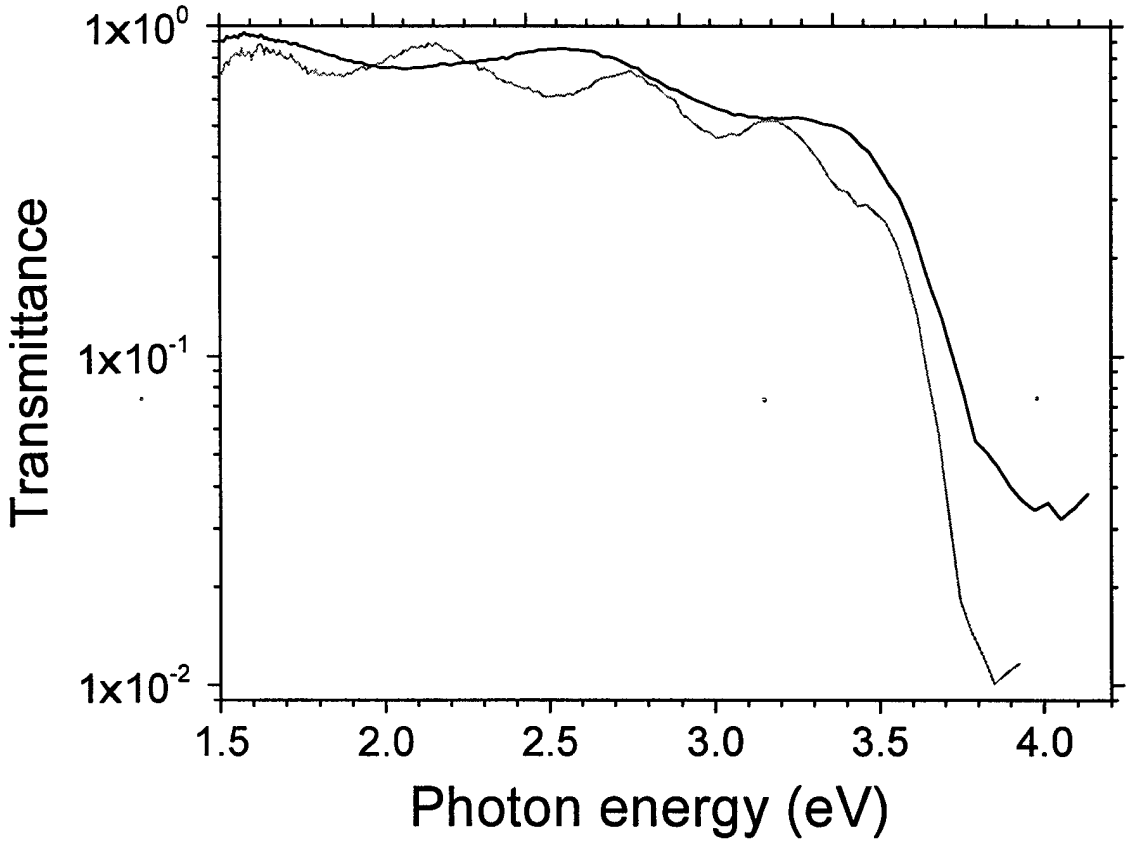

Figure 11. Comparison of transmittance data of PZT82 (in black) and PZT56 (in red). RTA at 800°C for 10 min in air.

PZT growth by sol-gel technique and structural characterization

Sol-gel method is cost effective and allows the change the composition of PZT thin films with ease. We investigated optimization of the sol-gel method such as spin-coating, dry, hydrolysis, and annealing in conjunction with PZT. PZT films were prepared using sol-gel method on $Pt(111)/TiO_2/SiO_2/Si$ substrates or $Ir(111)/Ti/SiO_2/Si$ substrates. The film deposition was performed by spin-coating of the PZT precursor at 4000 rpm for 40 s and then dried at 200°C on a hotplate for 5 min. These steps were repeated until the desired film thickness (180 nm) was obtained. The films were then pyrolyzed at temperatures ranging from 300°C to 400°C in order to remove the residual organic species, followed by a final crystallization step at higher temperatures in a preheated furnace in O_2 ambient.

Figure 12 (a) shows the X-ray diffraction (XRD) data of the sol-gel derived PZT films on $Pt(111)/TiO_2/SiO_2/Si$ substrate after annealing at temperatures from 650 to 750°C for 10 min under O_2 atmosphere. In this case, the pyrolysis process at 400°C for 2 min after each the drying step (200°C, 5min) was repeated. Although pyrochlore phase did not appear, the XRD patterns revealed that the PZT film was polycrystalline with (100) and (110) orientation under all annealing conditions. This is probably due to poorer crystalline quality of the e-beam evaporated Pt bottom electrode than the sputtered Ir bottom electrode to be discussed further below. The grain size tends to decrease slightly, and void fraction also decreases as the annealing temperature increases as shown in Figure 12(b).

A dramatic change in surface morphology and grin size of PZT film was observed through different heat treatment during pyrolysis steps as shown in Figure 13. In one process is that drying (200 °C, 5 min) and pyrolysis steps (400°C, 2 min) were repeated four times [see Figure 13(a)]. In the other the film already dried four times was pyrolyzed only once [see Figure **13**(b)]. The average grain size of the single-pyrolyzed PZT film was reduced by an order of magnitude as compared to that in the multiple-pyrolyzed PZT film. It should be noted that the voids [darker regions in Figure **13** (a)] between grains no longer exist in the single-pyrolyzed PZT film, implying that more uniform interface between PZT film and top electrode, resulting in better ferroelectric properties.[Appl. Phys. Lett. 75, 716 (1999), Appl. Surf. Sci. 169-170, 544 (2001)]

XRD patterns and surface morphologies of the sol-gel derived PZT films on sputtered Ir bottom electrode after the multiple-pyrolysis process [4 × (200°C, 5 min + 400°C, 2min)] followed by crystallization at 650°C, 700°C, and 750°C are shown in Figure **14**. XRD patterns of PZT films show (100)-preferred orientation under all annealing conditions although grain sizes decrease as annealing temperature decreases as shown in Figure **14**(b). As seen in the PZT/Pt case, voids are apparently reduced as the annealing temperature increases. It is noted that the grain size increases but smoothened at the higher annealing temperature which is opposite to the PZT/Pt case (Figure 12) although sample preparation conditions were the same. This is probably due to different initial surface conditions of the e-beam evaporated Pt layer which has poorer crystalline quality and rougher surface and sputtered Ir layer, resulting in possibly different nucleation kinetics during the thermal treatment. As compared to the PZT film on e-beam evaporated Pt bottom electrode discussed above, the intensity of (100) peak of PZT film is significantly increased as shown in Figure 14(a), implying sputtered Ir bottom electrode has initially better crystalline quality than the e-beam evaporated Pt bottom electrode.

Similar to the PZT film on Pt bottom electrode case discussed above, PZT films on Ir bottom electrode underwent single-pyrolysis steps under various conditions after repetiting the spin-coating and drying process 4 times. Each set of heat treatment conditions and their denotations are shown in Table IV. As shown in the XRD patterns of Figure **15**, in most cases, (100)-preferred orientation of PZT was obtained. A preliminary SEM investigation of surface morphologies of the corresponding PZT films (Figure 15) indicated that PZT films under D1P1 and D2P2 conditions show similar surface morphologies as well as microstructures while those under D1P2 and D2P3 show similarities What kind of similarities that are different from the aforementioned ones?, as shown in Figure 16. Unlike the multiple-pyrolyzed PZT/Ir case, the grain size was not sensitive to the annealing temperature, resulting in no improvement in reduction of void density in the film. However, it is noted that the different morphologies were observed between the two groups (D1P1-D2P2 and D1P2-D2P3); the SEM image of the latter group shows the evidence of partial erosion in the middle of the grains. This is probably due to a relatively short heat treatment period and/or low temperature during the drying process, leaving a slightly higher volume of organic materials in the film than needed. D1P1-D2P2 PZT films, thus, show better crystalline quality with single perovskite (100) phase while D1P2-D2P3 PZT films show mixture of (100) phase, (110) phase, or pyrochlore phase.

Figure 17(a) shows x-ray diffraction (XRD) patterns of sol-gel derived PZT films on $Ir/Ti/SiO_2/Si$ substrates which were single-pyrolyzed at 350°C and crystallized at 650°C, 700°C, and 750°C for 10 minutes

under O_2 atmosphere in a preheated furnace. All crystallized PZT films show the (100)-preferred orientation as seen in multiple-pyrolyzed PZT films in Figure 14 but a small portion of pyrochlore phase appeared at 33° for single-pyrolyzed PZT. As the annealing temperature increases, the relative XRD intensity of PZT (100) to pyrochlore phase reduces as shown in Figure 17(b) probably due to the relatively higher evaporation rate of Pb or PbO_2 at higher temperatures, e.g. 750°C, resulting in strengthening the pyrochlore phase in the PZT film. While grain size varied depending on the annealing temperature in the multiple-pyrolyzed PZT on Ir bottom electrode, grain size was insensitive to the annealing temperature for the single-pyrolyzed PZT films as shown in the SEM picture in Figure 17 (c). Void fraction (darker area in the SEM pictures) between grains in the single-pyrolyzed PZT film is significantly increased as compared to that in multiple-pyrolyzed PZT film (see Figure 14b). This is probably due to larger compressive strain for thicker(~240nm) PZT film which was pyrolyzed only once while multiple-pyrolyzed PZT film underwent a pyrolysis step per each layer (~60nm) deposition. Small areas in the middle of the grains in Figure 17 (c) seem related to higher evaporation rate of Pb or PbO_2 at annealing temperature of 750°C.

Table IV. Heat treatment condition for sol-gel PZT film on Ir bottom electrode.

Drying		Pyrolysis		Annealing	
D1	200°C, 2 min	P1	300°C, 10 min	A650	650°C, 10 min
D2	200°C, 10 min	P2	350°C, 10 min	A700	700°C, 10 min
		P3	400°C, 10 min	A750	750°C, 10 min

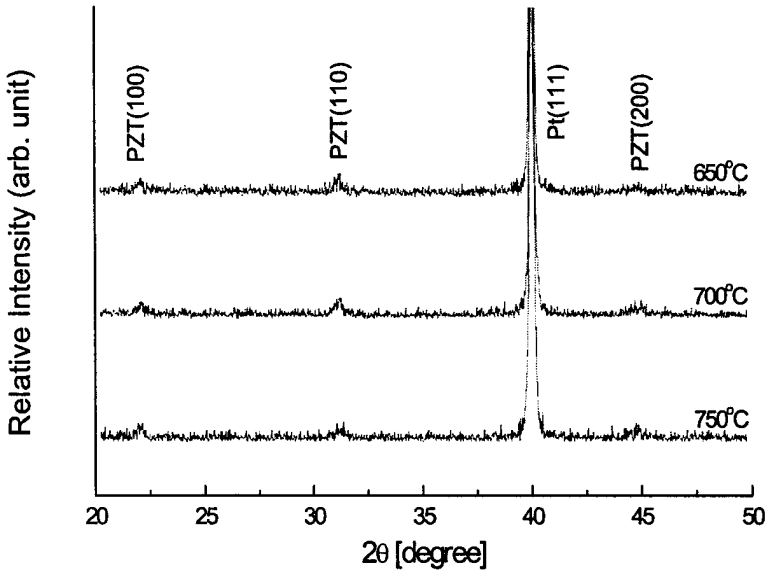

(a)

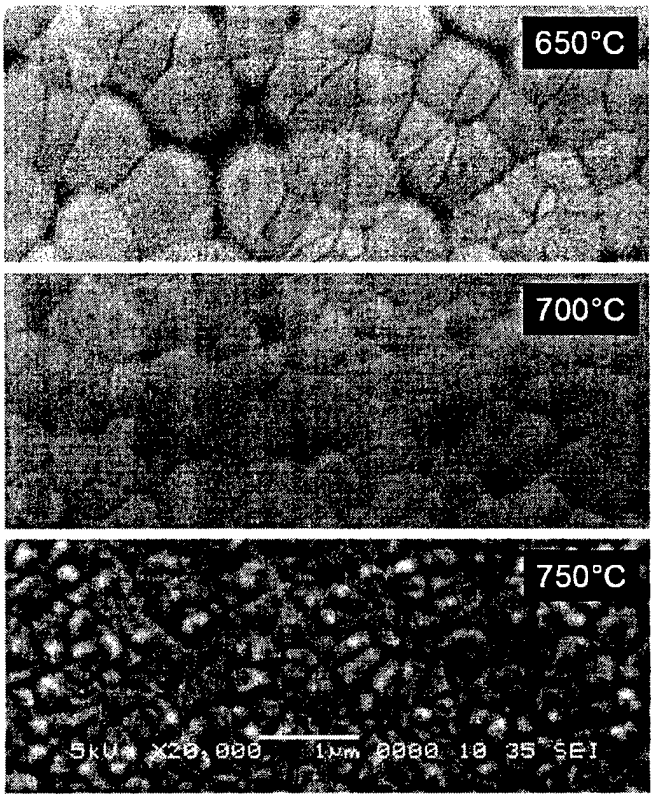

(b)

Figure 12. XRD patterns of sol-gel derived PZT films on Pt(111)/TiO_2/SiO_2/Si substrate after annealing at 650°C, 700°C, and 750°C after multiple-pyrolysis process at 400°C, (b) corresponding surface morphology of PZT films

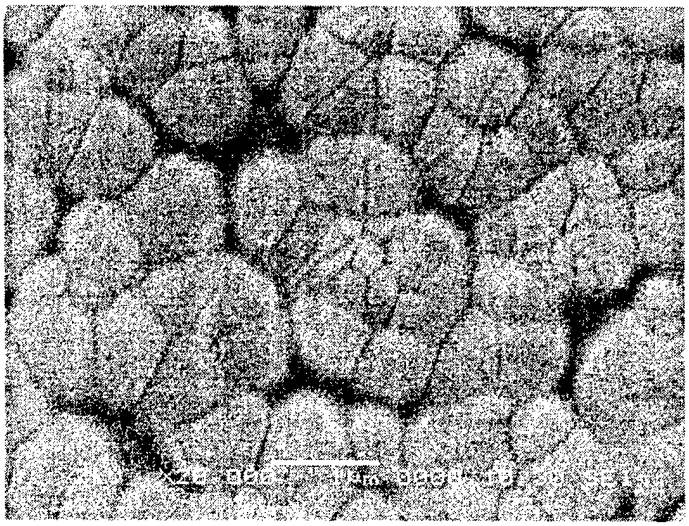

(a)

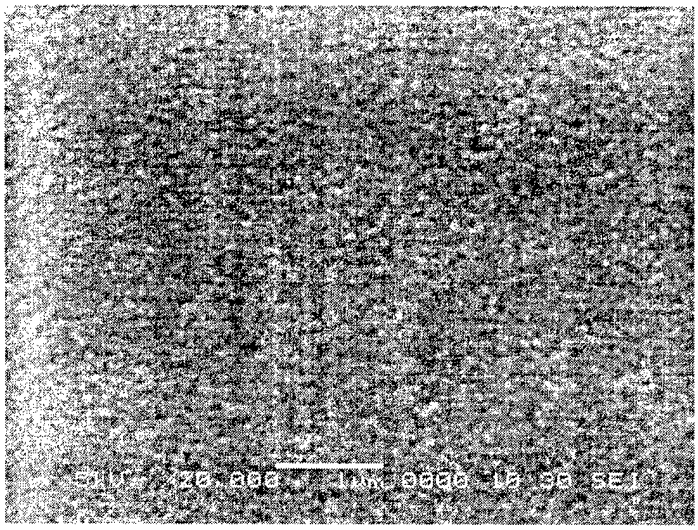

(b)

Figure 13. Surface morphology of sol-gel derived PZT film on Pt(111)/TiO_2/SiO_2/Si substrate (a) after multiple-pyrolysis [4 × (200°C, 5 min + 400°C, 2 min)], (b) after single-pyrolysis (200°C, 5 min × 4 + 400°C, 10 min) followed by crystallization at 650°C for 10 min under O_2 atmosphere.

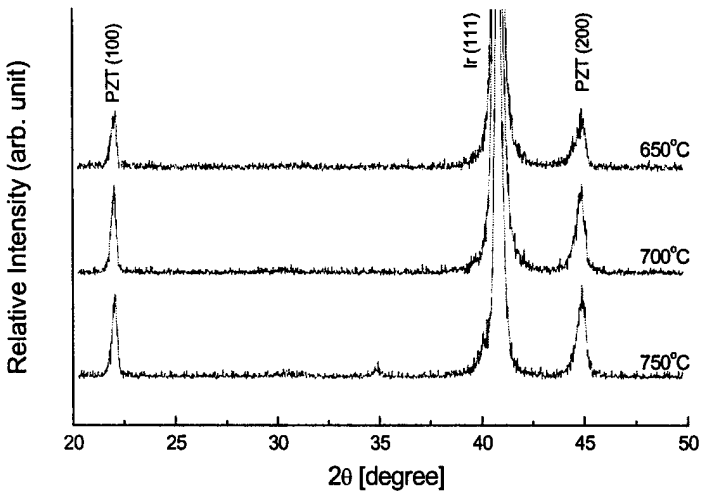

(a)

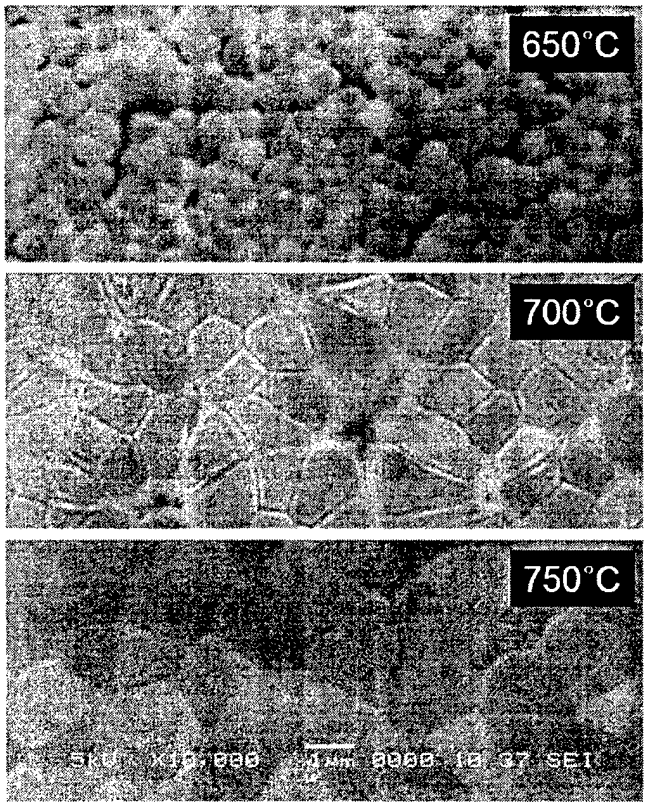

(b)

Figure 14. (a) XRD patterns of sol-gel derived PZT films on Ir(111)/Ti/SiO_2/Si substrate after annealing at 650°C, 700°C, and 750°C, indicating preferred (100) orientation, (b) corresponding surface morphology of PZT films.

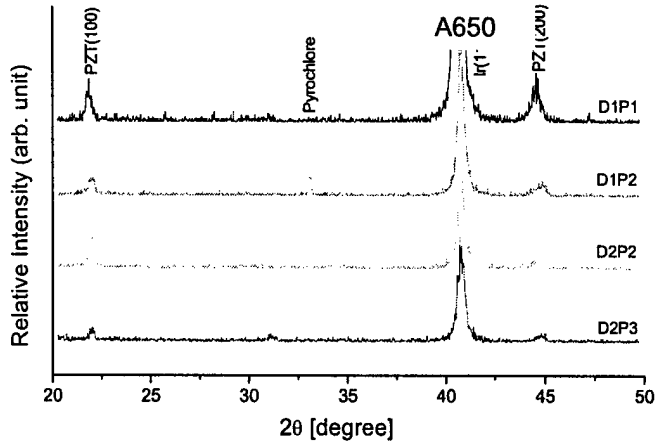

(a)

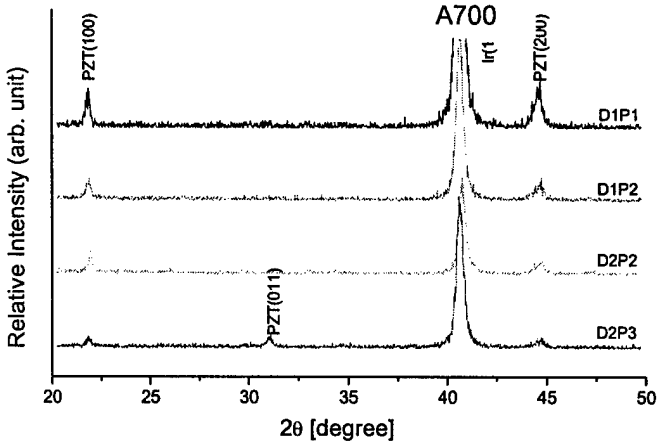

(b)

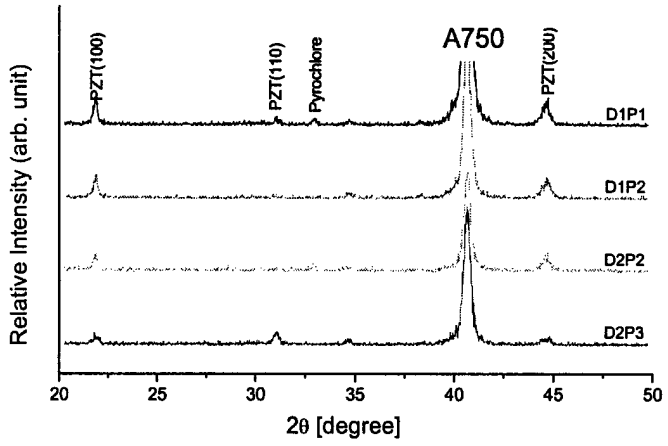

(c)

Figure 15. XRD patterns of PZT films on Ir(111)/Ti/SiO_2/Si substrate annealed at (a) 650°C (b) 700°C, and (c) 750°C after pyrolysis under various conditions

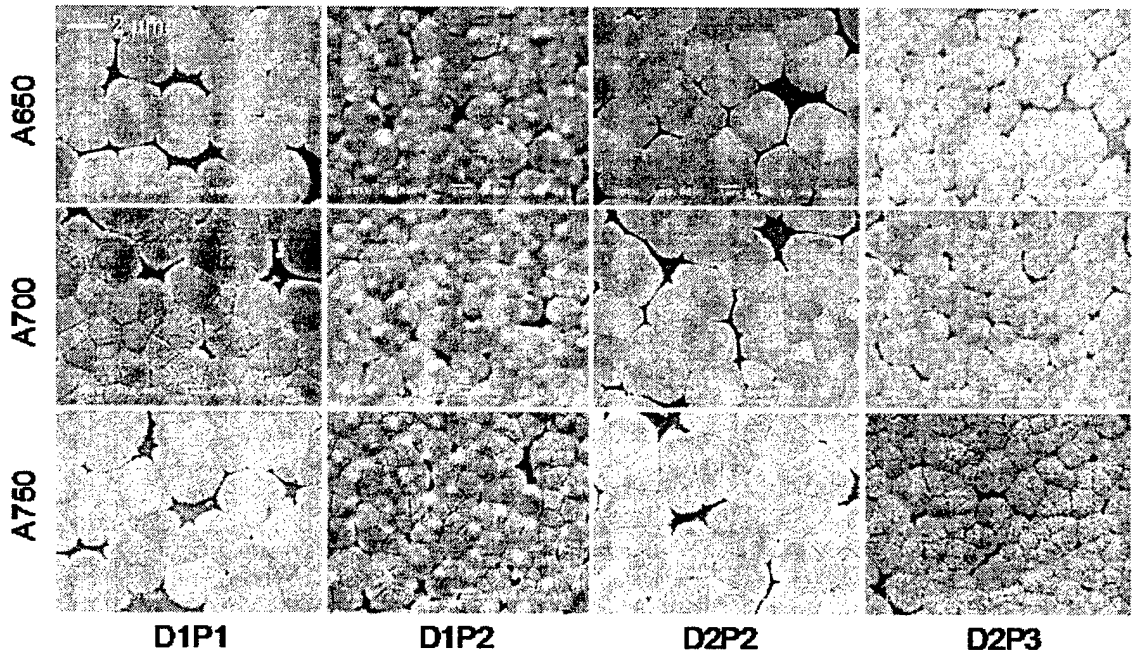

Figure 16. Surface morphology of PZT film on Ir(111)/Ti/SiO_2/Si substrate undergone various heat treatments.

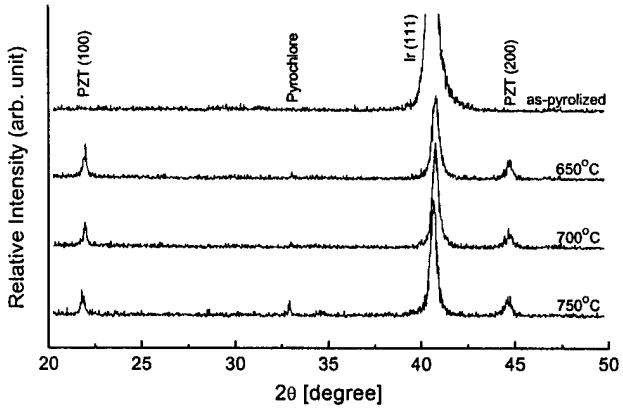

(a)

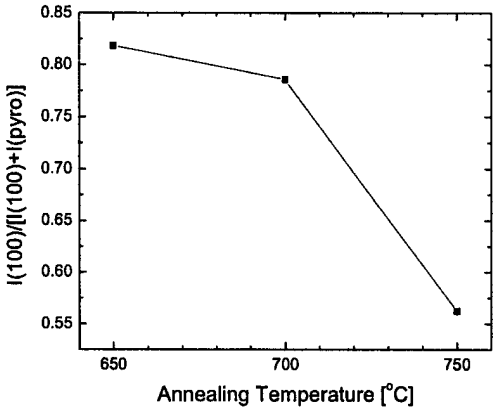

(b)

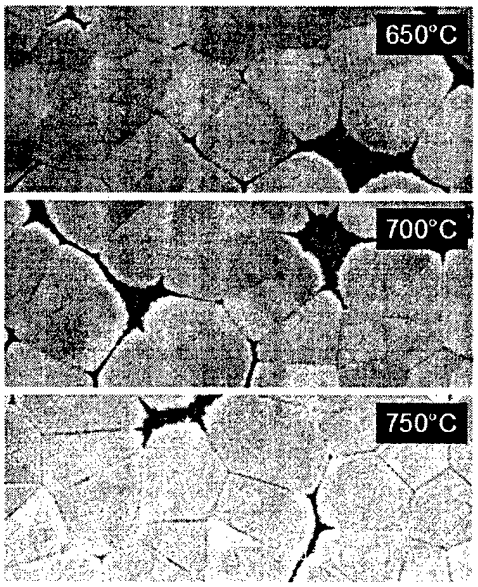

(c)

Figure 17. (a) XRD patterns of PZT/Ir films single-pyrolyzed at 350°C and crystallized at 650, 700, and 750 °C for 10 min under O_2 atmosphere in a preheated furnace, (b) the relative XRD intensity of PZT (100) as a function of annealing temperature.

Optical characterization (Spectroscopic Ellipsometry) of sol-gel PZT, PNZT, PLZT, and PLT.

Ex-situ spectroscopic ellipsometry (SE) data were taken for the sol-gel derived PZT samples and the imaginary part of the resultant pseudodielectric function is shown in Figure 18 (a). The redshift in $\langle\varepsilon_2\rangle$ spectrum below the photon energy of 4 eV is due to the increase in PZT film thickness as the annealing temperature increases. In the $\langle\varepsilon_2\rangle$ spectra, the light is strongly absorbed by the topmost layer of the PZT film above the energy band gap, approximately 4 eV, and thus the change in $\langle\varepsilon_2\rangle$ is very sensitive to the surface conditions[J. Vac. Sci. Technol. B 16, 2680 (1998)]. Decrease in $\langle\varepsilon_2\rangle$ above 4 eV implies that the surface is rougher probably due to higher evaporation rates of Pb or PbO_2, leaving more Pb and O vacancies in the PZT film as the annealing temperature increases. The SE data were fitted using a parametric semiconductor model. The extracted energy band gaps from the fit results and $\langle\varepsilon_2\rangle$ values at 5.3 eV are shown in Figure 18(b). With increasing annealing temperature, the same tendency of reduction in both $\langle\varepsilon_2\rangle$ and the energy band gap was observed. Furthermore, this trend is in good agreement with the relative XRD intensity of the PZT (100) shown in Figure 17 (b).

In addition to sputter grown PZT (PZT56 and PZT82) and sol-gel PZT, we also obtained $Pb_{0.98}Nb_{0.04}(Zr_{0.2}Ti_{0.8})_{0.96}O_3$ (abbreviated as PNZT), $Pb_{0.91}La_{0.09}(Zr_{0.65}Ti_{0.35})_{0.98}O_3$ (abbreviated as PLZT), and $Pb_{0.85}La_{0.15}Ti_{0.96}O_3$ (abbreviated as PLT) which were grown using sol-gel methods at Radiant Technologies. Refractive indices (n) and extinction coefficients (k) are important design parameters for optoelectronics. Information on electronic and phonon band structures is essential to understand the optical and electrical properties of the perovskite oxides. Dielectric fujnction ($\varepsilon = \varepsilon_1 + i\varepsilon_2$) is the square of the complex refractive indices ($N = n + ik$). We measured the dielectric functions of PZT, PNZT, PLZT, and PLT using spectroscopic ellipsometry (SE). Our spectroscopic ellipsometry included infrared (IR), visible (VIS), ultraviolet (UV), and deep-ultraviolet (DUV) spectral range. SE can estimate electronic and **phonon** This is because we are doing the IR and get the vibrational frequencies or what ???? band structures as well as refractive indices (Figure 19) and thicknesses. Using the VIS-UV-DUV data, we found that the lowest band peak near 4 eV in the dielectric function of PZTs is actually composed of two peaks (denoted as Ea and Eb), which are closely spaced. In addition we observed a higher energy peak (Ec) near 6.5 eV. Sol-gel derived PZTs have mainly the pyrochlore phase following spin coating and low temperature annealing, but transformed completely to perovskite phase after the high temperature anneal according to XRD investigations. Did I change the meaning here. If I did not the following sentence should read This phenomenon was corroborated in the SE data: the lowest peak near 4 eV is a single peak in the pyrochlore phase in films before the high temperature anneal and it became double peaks in the perovskite phase following the high temperature anneal. (Figure 20). Table V lists energy band gaps determined using parametric optical constant (POC) and standard critical point (SCP) models.

The SE data of IR spectral range are currently being analyzed to get information of IR-active phonons in PZT thin films. This information will help to verify the vibrational properties of PZT thin films.

(a)

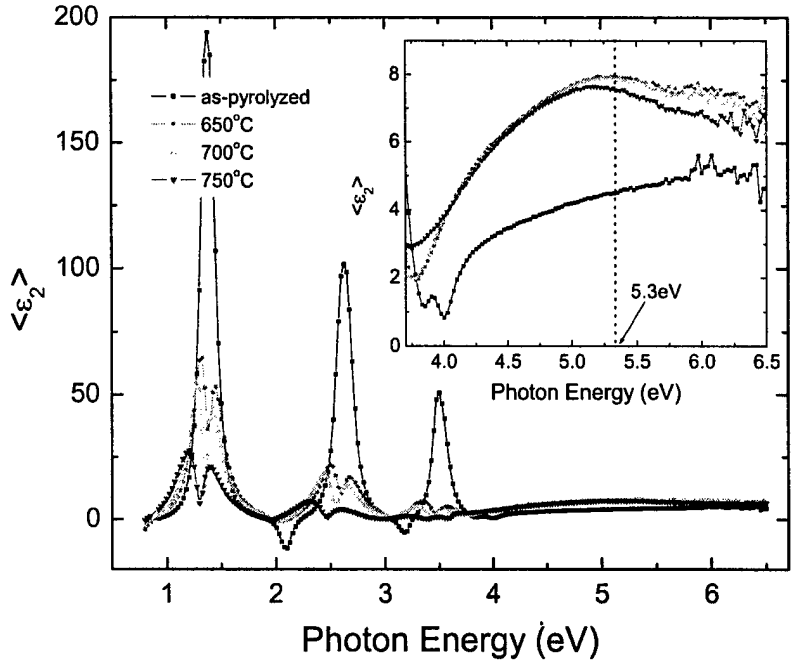

(b)

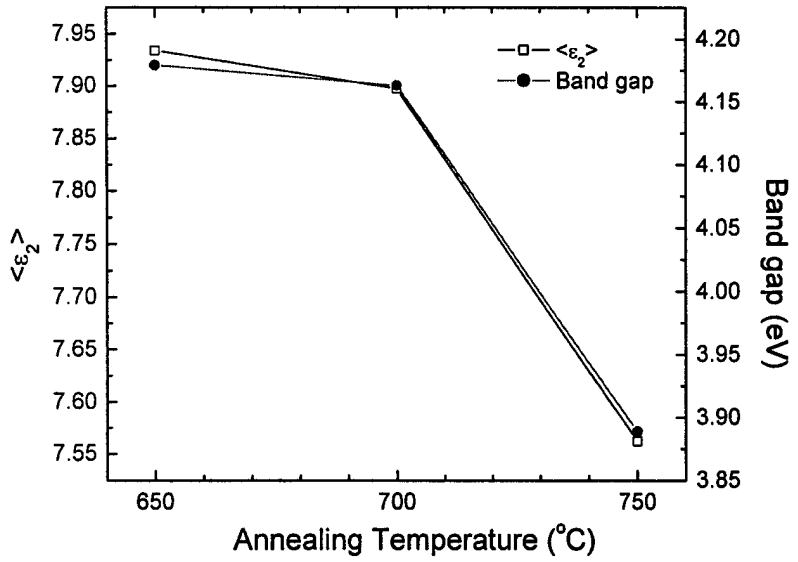

Figure 19. (a) Imaginary part of pseudodielectric function $<\varepsilon_2>$ of crystallized PZT/Ir film at 650, 700, and 750°C: the inset shows enlarged spectrum of $<\varepsilon_2>$ from 3.7 eV to 6.5 eV, (b) $<\varepsilon_2>$ values at 5.3eV in part (a) and fitted band gap as a function of annealing temperatures.

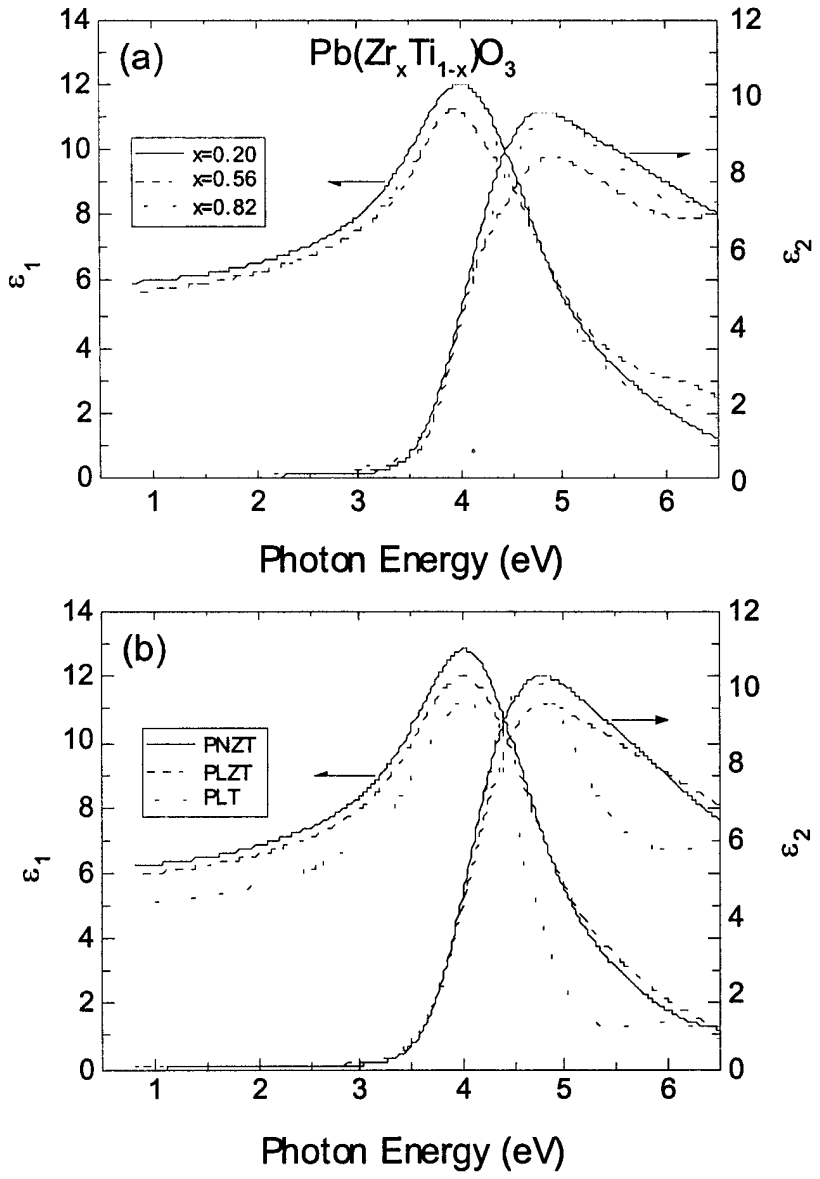

Figure 20. Dielectric function of the PZT layers in the spectral range of [0.8, 6.5] eV: (a) PZTs (b) PNZT, PLZT, and PLT

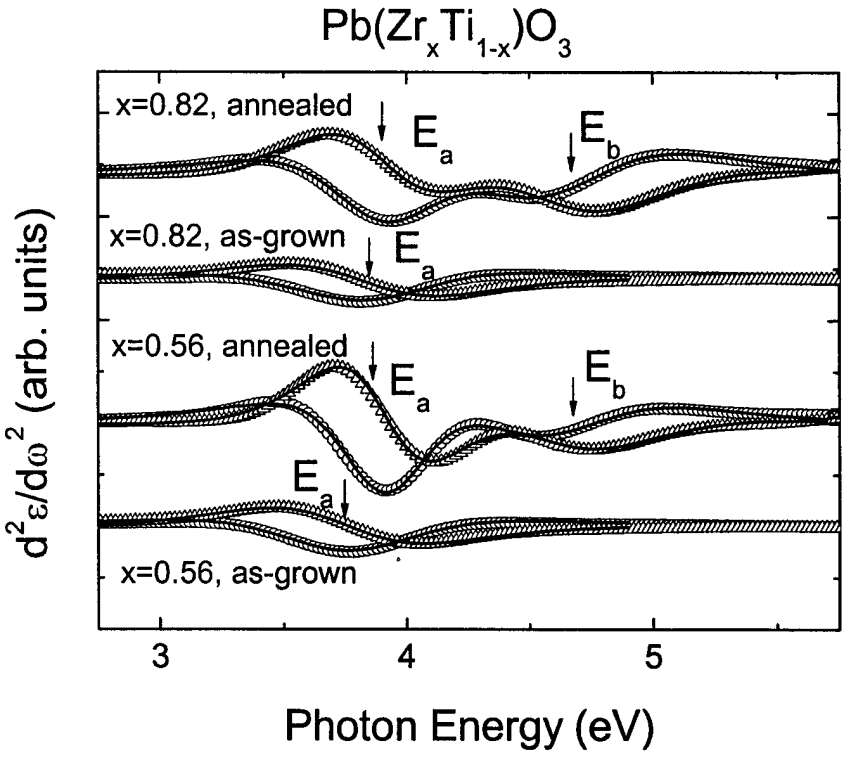

Figure 20. Comparison of the second derivative of the dielectric functions of as-grown and annealed PZT films grown on sapphire..

Table V. Energy band gaps determined using parametric optical constant (POC) and standard critical point (SCP) model

	E_a POC (SCP)	E_b POC (SCP)	E_c POC (SCP)
$Pb(Zr_{0.2}Ti_{0.8})O_3$	3.896 (3.872)	4.331 (4.379)	6.79 (6.79)
$Pb(Zr_{0.56}Ti_{0.44})O_3$, as-grown	3.767 (3.750)	3.804	6.66
$Pb(Zr_{0.56}Ti_{0.44})O_3$	3.922 (3.912)	4.464 (4.630)	6.06 (6.07)
$Pb(Zr_{0.82}Ti_{0.18})O_3$ as-grown	3.729 (3.854)	3.821	6.57
$Pb(Zr_{0.82}Ti_{0.18})O_3$	3.952 (3.904)	4.514 (4.667)	6.65 (6.71)
$Pb_{0.98}Nb_{0.04}(Zr_{0.2}Ti_{0.8})_{0.96}O_3$	3.983	4.287 (4.126)	6.79 (6.81)
$Pb_{0.91}La_{0.09}(Zr_{0.65}Ti_{0.35})_{0.98}O_3$	4.096 (4.081)	4.937	6.41 (6.74)
$Pb_{0.85}La_{0.15}Ti_{0.96}O_3$	4.196 (4.209)	4.835	6.54 (6.66)